

# Parallel transmission medical implant safety testbed: Real-time mitigation of RF induced tip heating using time-domain E-field sensors

Lukas Winter  | Berk Silemek  | Johannes Petzold  | Harald Pfeiffer |  
Werner Hoffmann | Frank Seifert | Bernd Ittermann 

Physikalisch-Technische Bundesanstalt (PTB), Braunschweig and Berlin, Germany

## Correspondence

Lukas Winter, Physikalisch-Technische Bundesanstalt (PTB), Biomedical magnetic resonance – 8.1, Abbestr. 2-12, Berlin 10587, Berlin, Germany.  
Email: lukas.winter@ptb.de

## Funding information

European Association of National Metrology Institutes, Grant/Award Number: 17IND01 MIMAS

**Purpose:** To implement a modular, flexible, open-source hardware configuration for parallel transmission (pTx) experiments on medical implant safety and to demonstrate real-time mitigation strategies for radio frequency (RF) induced implant heating based on sensor measurements.

**Methods:** The hardware comprises a home-built 8-channel pTx system (scalable to 32-channels), wideband power amplifiers and a positioning system with sub-millimeter precision. The orthogonal projection (OP) method is used to mitigate RF induced tip heating and to maintain sufficient  $B_1^+$  for imaging. Experiments are performed at 297MHz and inside a clinical 3T MRI using 8-channel pTx RF coils, a guidewire substitute inside a phantom with attached thermistor and time-domain E-field probes.

**Results:** Repeatability and precision are ~3% for E-field measurements including guidewire repositioning, ~3% for temperature slopes and an ~6% root-mean-square deviation between  $B_1^+$  measurements and simulations. Real-time pTx mitigation with the OP mode reduces the E-fields everywhere within the investigated area with a maximum reduction factor of 26 compared to the circularly polarized mode. Tip heating was measured with ~100  $\mu$ K resolution and ~14 Hz sampling frequency and showed substantial reduction for the OP vs CP mode.

**Conclusion:** The pTx medical implant safety testbed presents a much-needed flexible and modular hardware configuration for the in-vitro assessment of implant safety, covering all field strengths from 0.5-7 T. Sensor based real-time mitigation strategies utilizing pTx and the OP method allow to substantially reduce RF induced implant heating while maintaining sufficient image quality without the need for a priori knowledge based on simulations or in-vitro testing.

Lukas Winter and Berk Silemek contributed equally to this work.

This is an open access article under the terms of the Creative Commons Attribution License, which permits use, distribution and reproduction in any medium, provided the original work is properly cited.

© 2020 physikalisch-technische bundesanstalt. Magnetic Resonance in Medicine published by Wiley Periodicals LLC on behalf of International Society for Magnetic Resonance in Medicine

**KEYWORDS**

implant safety, interventional MRI, MR safety, open source hardware, orthogonal projection, parallel transmission

## 1 | INTRODUCTION

It is estimated that around 10% of the Western population, and an even higher fraction of MRI patients, are carrying medical implants.<sup>1</sup> Technological advancements and aging demographics will inevitably increase these numbers. This constitutes a challenge, because radio frequency (RF) induced heating of a metallic implant is a critical safety risk during an MRI exam. This holds for passive devices such as orthopedic implants,<sup>2</sup> stents<sup>3,4</sup> or cranial fixation plates,<sup>5</sup> active implantable medical devices including cardiac pacemakers<sup>6</sup> or deep brain stimulators (DBS)<sup>7-9</sup> or even the increasing number of implants without a medical purpose such as implanted radio frequency identification (RFID) devices or microchips.<sup>10</sup>

Standards on RF safety and MR compatibility testing of implants exist,<sup>11,12</sup> requesting questionable, since highly simplified (ASTM F2182), or very sophisticated and costly (ISO/IEC TS10974, tier 4) procedures. Both have in common however, that they test the implant ex ante in a highly artificial environment, a phantom setup or some virtual human reference subject. The specifics of the actual scan procedure, most importantly the individual patient anatomy but also exact implant location/trajectory, patient pose and position in the scanner, scanner type, RF excitation condition, MRI sequence, etc, are not part of the assessment. The ultimate goal of a widespread, fast and accurate safety assessment, performed in real-time for the specific patient in the scanner, cannot be achieved this way.

The inability to assess safety accurately, is a result of the many degrees of freedom to be considered and investigated, which makes a proper safety assessment by any ex ante approach a truly challenging endeavor.

Approaches to generalize the results of safety testing of medical implants exist and can be categorized in simulation based approaches,<sup>12-14</sup> electromagnetic measurements<sup>15,16</sup> MR-based measurements<sup>17-23</sup> or a combination of those.<sup>3</sup> Despite these important contributions to the field, we are still far away from a patient and exam specific assessment of implant safety in terms of accurate hazard predictions.

Other strategies are needed not only to assess RF induced currents and tissue heating, but also to mitigate them. Moving on from simple CP excitation to pTx systems proved to be a valuable asset to reduce RF induced currents and RF heating for safe operation<sup>24-28</sup> while maintaining diagnostic image quality.<sup>29,30</sup> An increase in RF transmission channels showed even more benefits for more complex lead/implant geometries.<sup>31,32</sup> These findings are encouraging, but so far, pTx is

still a research-only tool, hence costly, and further efforts are needed to prove its use. This includes a broader range of applications and availability of a robust technology.<sup>33-35</sup>

In the present work, a pTx-based implant safety testbed is presented. The testbed can be applied for RF heating experiments at all field strengths from  $B_0 = 0.5\text{T}$  to 7T and is easily scalable to 32 transmission channels. It furthermore enables programmed and automated probe or implant positioning with submillimeter accuracy inside a working volume of  $(55 \times 55 \times 65)\text{ cm}^3$ , which allows for 3D mapping experiments. We show that the pTx testbed can be applied within and without an MR scanner, allowing to validate field and temperature distributions using commercial RF coils in a realistic setting. For a widespread adoption and to facilitate reproducibility, the system will be published as open source hardware on [www.opensourceimaging.org](http://www.opensourceimaging.org). Using the pTx testbed together with a guidewire substitute, high precision thermistor readings ( $\sim 100\ \mu\text{K}$  resolution and 14Hz sampling frequency) and time-domain  $E$ -field sensor measurements, we furthermore introduce a real-time pTx mitigation strategy using the “orthogonal projection” method. With this method we demonstrate at 3T and 7T frequencies that RF induced tip heating can be reduced substantially while at the same time sufficient  $B_1^+$  is contained for imaging. This real-time pTx mitigation strategy relies on sensor measurements only, without the need to perform electromagnetic simulations.

## 2 | METHODS

The pTx implant safety testbed is shown in Figure 1.

### 2.1 | Signal transmission and reception

In the presented configuration, eight Tx channels are implemented using two 16-bit 4-channel arbitrary waveform generators (M4i.6622-x8, Spectrum Instrumentation GmbH, Grosshansdorf, Germany). The maximum sampling frequency of  $f_s = 625\text{ MHz}$  allows seamless RF transmission for frequencies up to  $f_0 = 128\text{ MHz}$  ( $B_0 = 3\text{ T}$ ). At 7T ( $f_0 = 297\text{ MHz}$ ) higher frequency spectral components would be generated (and amplified) very close to  $f_0$  at around  $328\text{ MHz}$  ( $f_s - f_0$ ), which would be difficult to suppress using a low pass filter. Therefore, a sampling frequency of 400 MHz is used for the 7T experiments, producing the target frequency of  $f_0 = 297\text{ MHz}$  ( $B_0 = 7\text{ T}$ ) plus a sideband signal

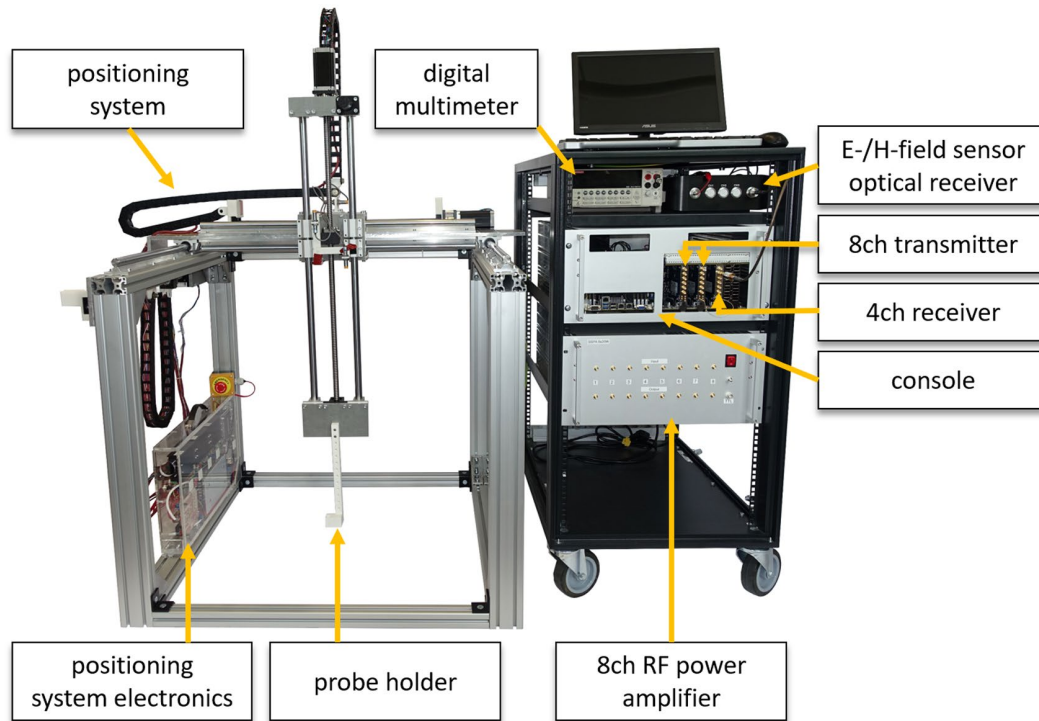


**FIGURE 1** Photograph of the parallel transmission medical implant safety testbed hardware assembled in a 19" (width = 55 cm, depth = 80 cm, height = 110 cm) rack. The depicted version consists of positioning system, 8-channel transmitter, 4-channel receiver, 8-channel broadband power amplifier module, digital multimeter and optical receiver and converter for the time-domain E- and H-field probes. The free space inside the rack can be utilized for a second 8-channel power amplifier module which allows a total of 16-channels in this compact configuration. The current hardware implementation as shown in the figure has a total cost of around 45 000€ (Excluding the E- and H-field sensors and the digital multimeter)

at 103 MHz. The latter is suppressed with a high-pass filter (passband, loss < 1.5 dB, 290-3000 MHz, SHP-300+, Mini-Circuits, New York, USA). For reception (Rx) a 14-bit 4-channel digitizer (M4i.4451-x8, Spectrum Instrumentation GmbH, Grosshansdorf, Germany) is used. Its maximum sampling rate is 500 MS/s. Up to  $B_0 = 3T$ , the digitizer can sample RF signals directly while obeying the sampling theorem. At 297MHz however, the signal level is reduced by about 6 dB by the anti-aliasing filter with a cut-off frequency of 260 MHz. Synchronization is supported for up to eight cards (Tx or Rx), allowing to scale up the system to up to 32 channels. Both transmission and reception cards use an PCI Express x8 Gen2 Interface. The signals generated by the arbitrary waveform generator cards are proportional to  $\cos(\omega t + \phi)$  which defines the transmit phases. The received signals are multiplied by  $e^{i\omega_{LO}t}$  during digital down conversion.

## 2.2 | RF power amplifier

For power transmission, eight broadband (20 MHz-1 GHz) RF power amplifiers (RFPAs) with 50 dB gain (ZHL-20W-13SWX+, Mini-Circuits, New York, USA) are utilized

allowing for a peak of  $P_{out} = 20$  W per channel with 100% duty cycle. The RFPAs are assembled in a casing with power supply, cooling fans, manual TTL switch and TTL input for blanking.

## 2.3 | RF coil

For our study, a 7T 8-channel Tx/Rx head coil was used.<sup>36</sup> It is made of eight rectangular loops (length = 160 mm) in an elliptical arrangement (anterior-posterior distance: 250 mm, left-right distance: 215 mm) and a cylindrical RF shield.

## 2.4 | Phantom

A cylindrical polymethyl methacrylate (PMMA) tube (inner diameter = 200 mm) with a sealed bottom was filled up to a level of 188 mm with a mixture of polyvinylpyrrolidone (PVP), deionized water and NaCl. Permittivity and conductivity were measured as  $\epsilon = 36$  and  $\sigma = 0.27$  S/m, respectively, at 297 MHz. PVP is nontoxic, sufficiently viscous to suppress convection, has a single-line spectrum and easily adjustable permittivity and conductivity. All of this makes it

a very favorable MR phantom material.<sup>37-40</sup> The cylinder allows free access from the top such that implants, and sensors can easily be inserted and repositioned in the phantom liquid.

## 2.5 | Sensor measurements and reproducibility

Four sensor configurations have been tested in this work. Time-domain  $E$ -field and  $H$ -field sensors (E1TDSxSNI and H1TDSx, Speag, Zurich, Switzerland), fiber-optic temperature probes (Luxtron, Lumasense Technologies, Santa Clara, USA) and a high resistance ( $R_{25^{\circ}\text{C}} = 10\text{ k}\Omega$ ) negative-temperature-coefficient thermistor (NCP 18XH103F03RB, Murata Manufacturing, Nagaokakyo, Japan). Fiber-optic temperature probes are widely used for RF safety testing, they are MR compatible and immune to the RF field. They have limitations, however, in precision and sampling speed. Thermistor probes, on the other hand, are known to be faster and more precise but may be severely affected by the incident RF field.<sup>41</sup> In the  $E$ -field sensor (bandwidth 10 MHz-6 GHz),  $E$ -fields (amplitude and phase) are detected by a 3 mm dipole at its tip, converted to an optical signal and transferred to a receiver via a fiber-optic cable. The optical receiver converts the optical back to an RF signal that is fed to one channel of the receiver card for digitization.  $E$ -field probes were successfully implemented previously in validation and implant safety related experiments.<sup>42-45</sup> The  $H$ -field sensor operates similarly using a loop instead of a dipole. A  $90^{\circ}$  rotation of

the  $H$ -field sensor is needed to measure  $H_x$  and  $H_y$  and calculate  $B_1^+$ . Using this technique,  $B_1^+$  was measured at 297 MHz in a (60 mm  $\times$  60 mm) slice in the  $x$ - $y$  plane at a  $z$  position 50 mm below the phantom liquid surface with an in-plane resolution of 5 mm. Inside this central area,  $B_z$  is negligible compared to  $B_x$  and  $B_y$ , thus allowing to validate all relevant field components with minimal error based on  $B_1^+$  measurements (Supporting Information Figure S1). The measured values were compared to electromagnetic (EM) field simulations (Sim4Life v5.0, ZMT Zurich MedTech AG, Zurich, Switzerland) of the RF coil and phantom. All lumped-element capacitors in the simulations had the true values from the physical coil and the complex matching impedance of the eight ports was adjusted to achieve an S-matrix as close as possible to the measured one.<sup>36</sup>

For RF heating experiments, a semi-rigid coaxial cable (total length = 177 mm, diameter = 4 mm, 15 mm of the outer conductor isolation removed at the tip) was used as a dummy implant resembling a guidewire for medical intervention. At the tip of this guidewire substitute, a thermistor was soldered between inner and outer conductor (Figure 2), thus allowing sensitive temperature measurements directly at the tip. At the remote end, the coaxial guidewire was connected with a coaxial cable to a digital multimeter (Keithley 2000, Tektronix, Beaverton, USA) for precise measurements of the temperature dependent resistance. To suppress artifacts due to stray RF on the cable, low pass filters (SLP-1.9+, DC-1.9MHz, Mini-Circuits, New York, USA) were used at the guidewire connection terminal and at the input to the multimeter. The

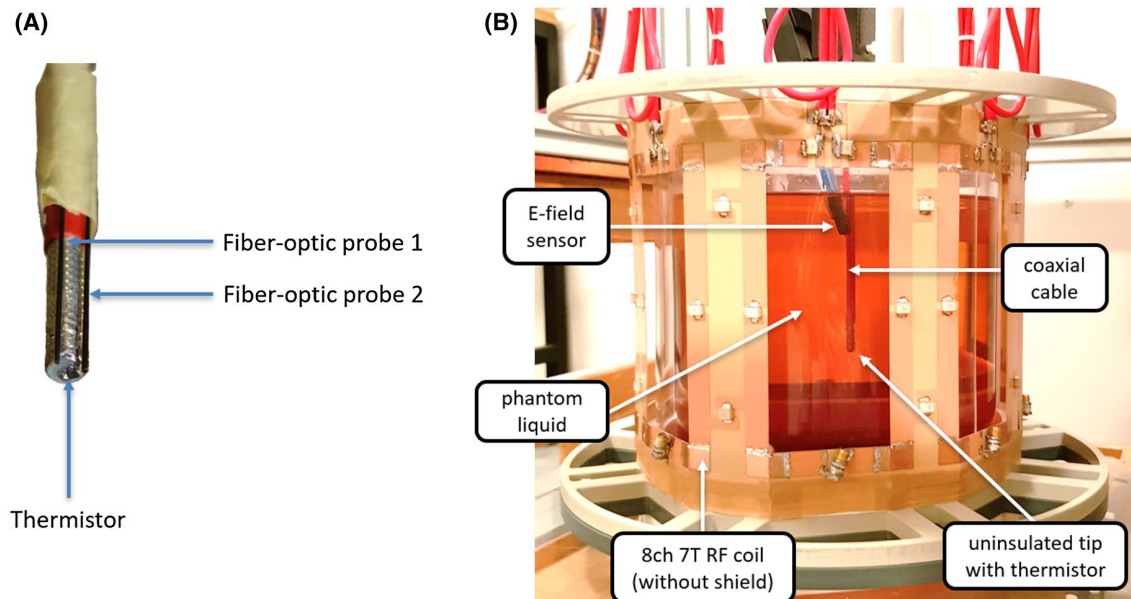


**FIGURE 2** A, Photograph of the coaxial semirigid cable as a dummy guidewire with the connected thermistor and the position of two fiber-optic temperature probes. At the tip the outer insulation of the cable has been stripped at a length of 15 mm. B, Photograph of the measurement setup at 297 MHz of the guidewire substitute in the phantom placed inside the 8-channel 7T pTx RF coil (with the cylindrical RF shield removed to visualize the experimental setup). The  $E$ -field sensor is positioned close to the guidewire and about 65 mm away from the tip to allow measurements of the  $E$ -field component perpendicular to the guidewire

measured resistance values were transmitted to the console over a serial connection.

To evaluate repeatability and accuracy of the system the following measurements were performed:

- (i) Repeatability of the RF transmission/reception system was investigated by subsequently transmitting 10 RF pulses of 1ms duration and measuring the received  $E$ -field amplitude.
- (ii) Repeatability of the positioning system was investigated by repositioning the probe 10 times to the same location and transmitting the same RF pulse of 1 ms as in (i).
- (iii) Repeatability of the thermistor measurements was investigated by transmitting ten times a set of 64 pTx heating pulses with different amplitude and phase contributions, each of 2s duration followed by a 2s cooling period. Each pulse produced a distinct incident RF field.

In order to assess the accuracy of our measurement system an uncertainty analysis according to ISO/TS 10974 and ISO/TR 21900 was performed.<sup>12,46</sup> The results are summarized in Table S1.

## 2.6 | Positioning system

For precise, reproducible and automated positioning of the guidewire-sensor assembly, the open-source hardware 3D positioning system COSI Measure was used.<sup>47</sup> A wireless Bluetooth connection was established between positioning system and Tx/Rx console to steer the positioning system from within the pTx implant safety testbed console and to allow automated mapping.

## 2.7 | TEM calibration cell

The known, homogeneous and unidirectional field of a transverse electromagnetic (TEM) cell<sup>48</sup> was used to calibrate and quantify the time-domain  $E$ -field and H-field sensor readings. The TEM cell field uncertainty is  $\pm 5\%$  (Supporting Information Table S1). All field probe calibrations were performed in air.

## 2.8 | Console

The console uses a X10DRX motherboard (Supermicro Computer Inc, San Jose, USA) with 10x PCI-Express 3.0  $\times$  8 slots controlled by two CPUs. This allows to accommodate a total of  $10 \times 4 = 40$  channels, eg, 32 Tx plus 8 Rx channels. The console runs on Linux and communicates with the Tx/Rx cards via PCI Express.

## 2.9 | Real-time mitigation of RF induced heating using the 'orthogonal projection method'

To demonstrate RF induced heating and its mitigation using pTx, the guidewire substitute was positioned at various locations inside the RF coil. The RF induced currents in the guidewire result in elevated SAR around the tip and this increase scales quadratically with the induced current close to the tip.<sup>14</sup> Minimizing or reducing this current therefore reduces RF-induced heating at the tip. This has been demonstrated previously using pick-up coil measurements to detect RF coupling of a guidewire<sup>49,50</sup> or current sensors on the guidewire.<sup>16,26,28,51</sup> Here we use a time-domain  $E$ -field sensor close to the guidewire (radial distance  $\approx 1$  mm) but 65 mm away from its tip in  $z$  (distal) direction. The distance between tip and sensor was chosen to guarantee an emergence of the  $E$ -field sensor tip in the phantom liquid during measurements in order to avoid spurious field contributions. The sensor is oriented perpendicular to the guidewire where  $E_{tan} \approx 0$  (incident plus scattered  $E$ -field) (Figure 2). We therefore measure the complex valued (magnitude and phase) amplitude  $E_r$  of the radial  $E$ -field component generated when the RF coil is driven by a complex steady-state excitation voltage vector:

$$\vec{u} = k \times (u_1, u_2, \dots, u_8) \quad (1)$$

Hereby, the complex vector element  $u_i$  describes the applied sinusoidal voltage at channel  $i$  for a given constant phase reference while the normalization factor  $k \in \mathbb{R}$  is chosen such that the same transmitted forward power

$$P_0 = \frac{|\vec{u}|^2}{8Z_0}, Z_0 = 50\Omega \quad (2)$$

is achieved for all cases. At each measurement location eight voltage vectors

$$\begin{aligned} \vec{u}_1 &= k_1 \times (1V, 0, \dots, 0), \vec{u}_2 = k_2 \times (0, 1V, 0, \dots, 0), \dots, \vec{u}_8 \\ &= k_8 \times (0, \dots, 0, 1V) \end{aligned} \quad (3)$$

with an overall average forward power of  $P_{rms} = 1.4$  W over a total duration of 1.28 ms are subsequently applied and the resulting  $E_r$  is measured with the  $E$ -field sensor. These eight measurements form an 8-dimensional complex valued vector

$$\vec{S}_{TDS} = (E_r(\vec{u}_1), E_r(\vec{u}_2), \dots, E_r(\vec{u}_8)) \quad (4)$$

where the subscript TDS refers to time-domain sensor. Three excitation scenarios were investigated:

1. Circularly polarized (CP) mode:

$$\begin{aligned}\vec{u}_{CP} &= k_{CP} \times (u_1, \dots, u_n, \dots, u_8), u_n \\ &= \exp\left(-\frac{2\pi i}{8} \cdot n\right), 1 \leq n \leq 8, \quad n \in \mathbb{N},\end{aligned}$$

ie, equal amplitudes and  $45^\circ$  phase increment per channel. With respect to both image uniformity and implant related hazard the CP mode represents the excitation condition of a standard scanner body coil without pTx capabilities.

2. Worst-case (WC) mode:  $\vec{u}_{WC}$ , ie, phases are set for coherent superposition and voltage amplitudes are set proportional to the measured  $E$ -field sensor signals for each channel, in other words  $\vec{u}_{WC} \propto \vec{S}_{TDS}$ . The WC mode has little practical relevance for imaging, however it *can* be produced by a pTx system and is thus important in the context of safety assessments.
3. Orthogonal projection (OP) mode:  $\vec{u}_{OP}$  is obtained by projecting  $\vec{u}_{CP}$  onto the subspace orthogonal to  $\vec{u}_{WC}$ <sup>52</sup>

$$\vec{u}_{OP} = \hat{u}_{CP} - \hat{u}_{WC} (\hat{u}_{WC} \cdot \hat{u}_{CP}) \quad (5)$$

where  $\hat{u}_{CP}$  and  $\hat{u}_{WC}$  are the normalized CP and WC excitation vectors, respectively:

$$\hat{u}_{CP} = \frac{\vec{u}_{CP}}{\|\vec{u}_{CP}\|}, \quad \hat{u}_{WC} = \frac{\vec{u}_{WC}}{\|\vec{u}_{WC}\|} \quad (6)$$

$$\Rightarrow \hat{u}_{CP} \cdot \hat{u}_{CP} = \hat{u}_{WC} \cdot \hat{u}_{WC} = 1 \quad (7)$$

By construction, the OP mode aims to provide both implant safety by avoiding the WC mode in going to the orthogonal subspace  $\vec{u}_{OP} \perp \vec{u}_{WC}$  and acceptable image quality by remaining as close as possible to the CP mode. It is a “best compromise” mode.

Within the investigated framework, consistently the worst-case mode generates the highest and the orthogonal projection mode the lowest induced  $E$ -field values. Since the orthogonal projection mode is calculated from  $E$ -fields measured at the sensor position 65 mm away from the tip, it is not a priori clear how well it mitigates any hazards at the guidewire tip, where highest SAR and RF induced heating are expected. Temperature measurements directly at the tip were thus performed to investigate this relation. To illustrate the spatial distribution of the induced signals for the WC, CP and OP modes, an area of (100 mm  $\times$  50 mm) was mapped with 5 mm spatial resolution in an  $x$ - $y$  plane through the tip of the guidewire, ie, 90 mm below the liquid surface. For the mapping all transmission modes ( $\vec{u}_{WC}$ ,  $\vec{u}_{CP}$ ,  $\vec{u}_{OP}$ ) were normalized to the same transmitted forward power  $P_{\text{rms}} = 1.4$  W.

In order to demonstrate that the OP mode delivers suitable image quality, while reducing tip heating at the

same time, EM simulations (XFDTD 6.4, Remcom Inc, State College, USA) and temperature simulations were performed with the human voxel model Ella.<sup>53,54</sup> For the temperature simulations, Pennes' Bioheat Equation was implemented, and the steady-state temperatures were determined for a total forward power of  $P_{\text{in}} = 20$  W. The thermal conductivity of the implant was neglected for a conservative assumption.

## 2.10 | pTx mitigation and imaging at 3T

The pTx implant safety testbed and orthogonal projection method were tested in a 3T MR environment (Verio, Siemens Healthineers, Erlangen, Germany). A 3T 8-channel pTx RF coil (RAPID Biomedical, Rimpf, Germany) was used for transmission into a (200 mm  $\times$  260 mm  $\times$  35 mm) PVP phantom with a guidewire substitute positioned 45 mm away from the side of the phantom (Figure 3A,B). A 260 mm long rod holding the  $E$ -field sensor was connected to the positioning system, which was located at the end of the patient table (Figure 3A), allowing to map the induced  $E$ -fields at the guidewire at various locations. The OP method and RF heating experiments (WC, CP and OP) were investigated in two configurations:

- a. Transmitting with the home built pTx system, which was connected over the filter plate outside of the MR scanner room (Figure 3C), WC, CP and OP modes were determined, and induced  $E$ -fields were measured along the guidewire (10mm steps over a total distance of 140 mm). RF heating experiments were performed using WC, CP and OP mode determined at an  $E$ -field sensor location 90mm away from the tip.
- b. Transmitting with the commercial 8-channel pTx system (Siemens Healthineers, Erlangen, Germany) and a 2D GRE sequence (sinc pulse),  $S_{TDS}$  and consequently WC, CP and OP mode were determined based on  $E$ -fields measured 110 mm away from the tip. RF heating experiments were performed with the GRE sequence (Total time = 50 seconds, 55V peak pulse amplitude, TR = 4.5 ms). MR images of CP and OP mode excitation were acquired.

## 3 | RESULTS

### 3.1 | In-silico and in-vitro assessment of RF fields

$B_1^+$  maps calculated from EM field simulations and temperature simulations inside the voxel model Ella for CP and OP mode are shown in Figure 4. Baseline temperature

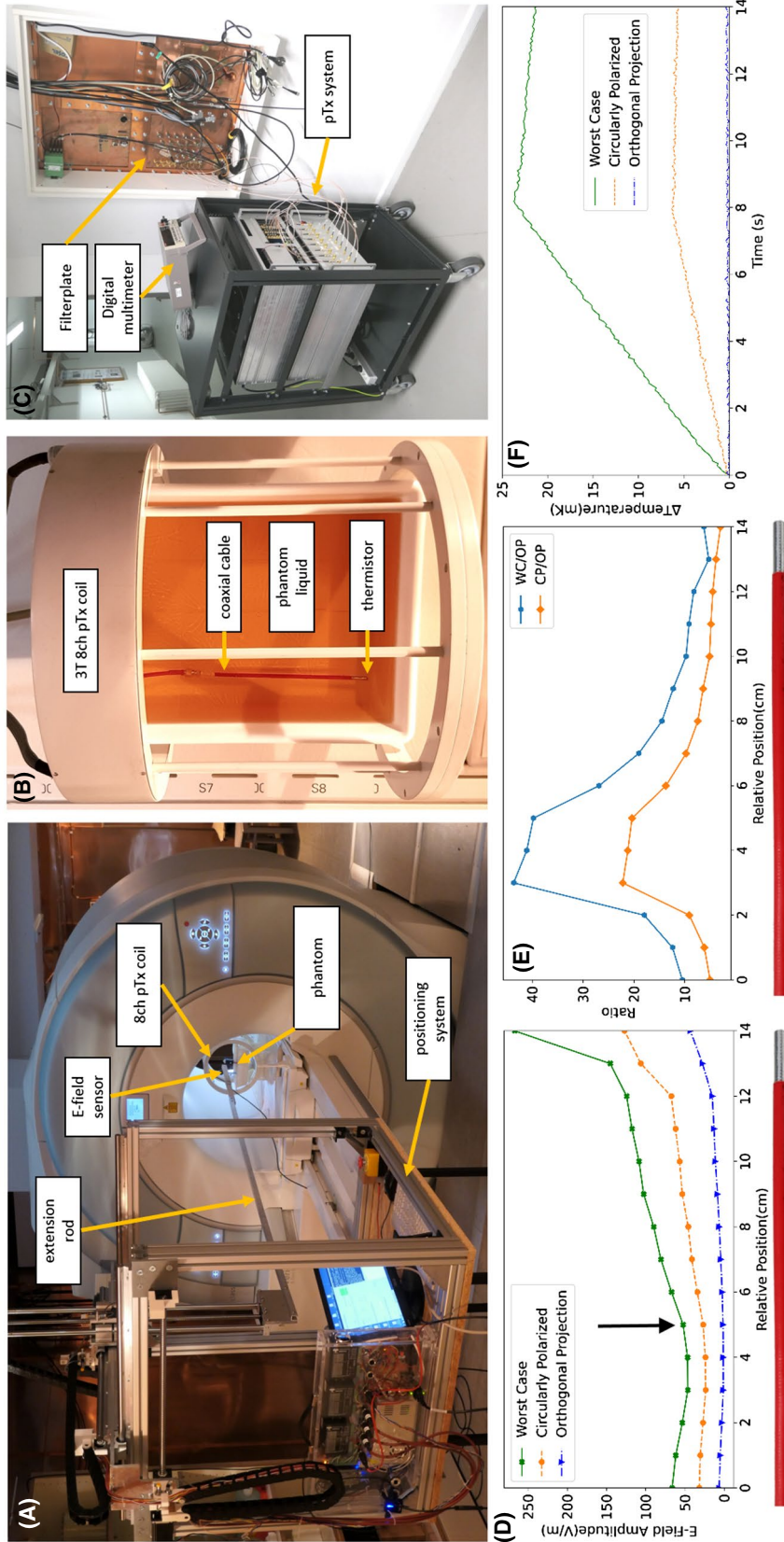


**FIGURE 3** A and B, Photographs of the measurement setup inside a 3T MRI using the pTx implant safety testbed. An extension rod (A) was used to hold the E-field sensor and measure the induced radial E-field along the coaxial cable embedded in the phantom liquid (B). The console, power amplifiers and digital multimeter were located outside the scanner room and were connected through the filter plate (C) to the 8-channel pTx RF coil and the coaxial cable and the coaxial cable and the coaxial cable and OP transmission based on E-field sensor measurements acquired with the home-built pTx system of 15 locations along the coaxial cable and (E) location dependent ratios WC/OP and CP/OP. F, RF heating experiments based E-field sensor measurements 90mm away from the tip (black arrow in (D)) showing that the determined OP mode is substantially reducing tip heating compared to CP and WC

was 37°C. For the CP mode, the tip temperature is 38.2°C, while the OP mode has a maximum temperature of only 37.3°C and does not indicate an implant related increase of the brain temperature around the tip (Figure 4). At the same time  $B_1^+$  was not influenced strongly during OP excitation ( $B_{1OP\_center}^+ = 18.6\mu T/\sqrt{kW}$ ) in the central region of the brain versus CP excitation ( $B_{1CP\_center}^+ = 21.2\mu T/\sqrt{kW}$ ).

Simulated and measured  $B_1^+$  fields in the phantom are shown in Figure 5. The root-mean-square difference for the mapped area was 6.3% indicating a good correlation of the results. The simulated  $B_1^+$  field indicate a maximum of  $25.7\mu T/\sqrt{kW}$ , whereas the overall measured maximum of the  $B_1^+$  field was  $27.9\mu T/\sqrt{kW}$  (Figure 5C-F). The mean absolute difference between measured and simulated  $B_1^+$  was  $2.46 \pm 1.24\%$  along a line in x-direction (Figure 5E) and  $2.65 \pm 0.89\%$  along a line in y-direction (Figure 5F).

### 3.2 | Reproducibility and precision

Ten repeated  $E$ -field measurements on the guidewire substitute resulted in a mean standard deviation of about 1.1%. Repositioning the guidewire at the same location ten times increased the variability to a mean deviation of 2.6%.

Comparative temperature measurements of the fiber-optic probes and the thermistor are displayed in Figure 6. The fiber-optic probes measure the baseline temperature increase accurately, precision ( $\sim 0.5^\circ\text{C}$ ) and temporal resolution (1s) are limited, however. The thermistor, in contrast, depicts the temperature accurately with much higher precision ( $\sim 100\mu\text{K}$ , noise level  $< 50\mu\text{K}$ ) and temporal resolution ( $\sim 70\text{ms}$ ). Compared to the fiber-optic sensor the thermistor requires much less RF power and/or heating duration for a robust measurement and allows therefore a fast and precise

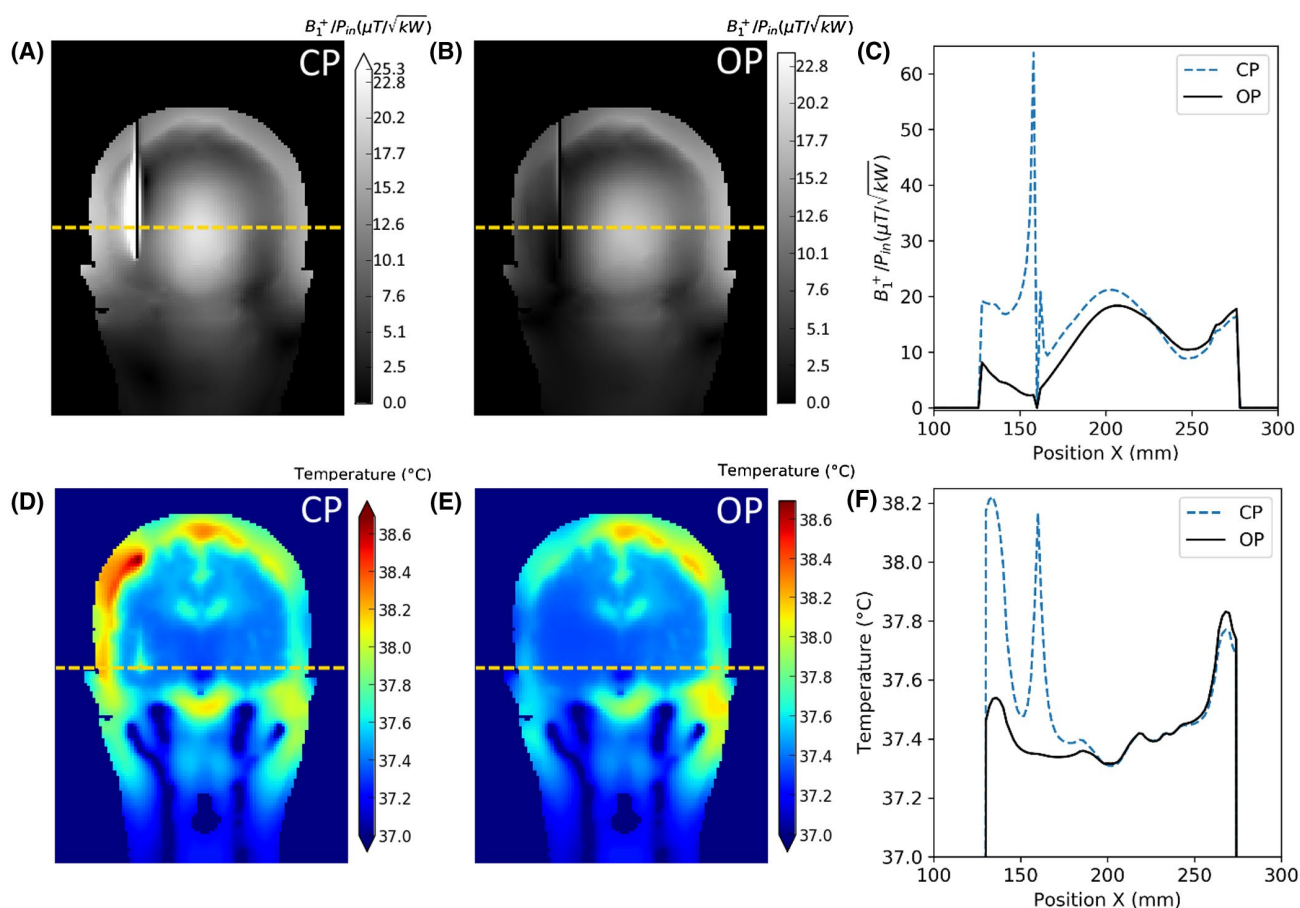


**FIGURE 4** A and B,  $B_1^+$  ( $f = 297\text{ MHz}$ ) and (D-E) temperature simulations of a coronal slice of the human voxel model Ella with an inserted uninsulated wire into the brain for CP and OP mode excitation. For the simulations, single port excitation FDTD runs were performed with an own co-simulation framework and an own stable GPU accelerated thermal solver (Pennes Bioheat equation including thermal conduction, metabolic heat, perfusion and large vessels as heat sinks).<sup>52</sup> All material parameters were adjusted based on the IT IS' database<sup>54</sup> (C)  $B_1^+$  and (F) temperature profiles for CP and OP mode along the yellow dotted line in axial direction. The OP mode effectively suppresses  $B_1^+$  artifacts near the wire, while the overall  $B_1^+$  distribution (eg, central region of the brain) is only moderately affected, which renders MR imaging feasible. At the same time tip heating is reduced substantially for the OP mode in comparison to the CP mode. An absolute comparison of MR based  $B_1^+$  maps with the simulations of the RF coil (including channel coupling, intrinsic RF coil losses, cable losses, T/R switch and RF plug losses) was performed previously with discrepancies of 5%-10%.<sup>36</sup>

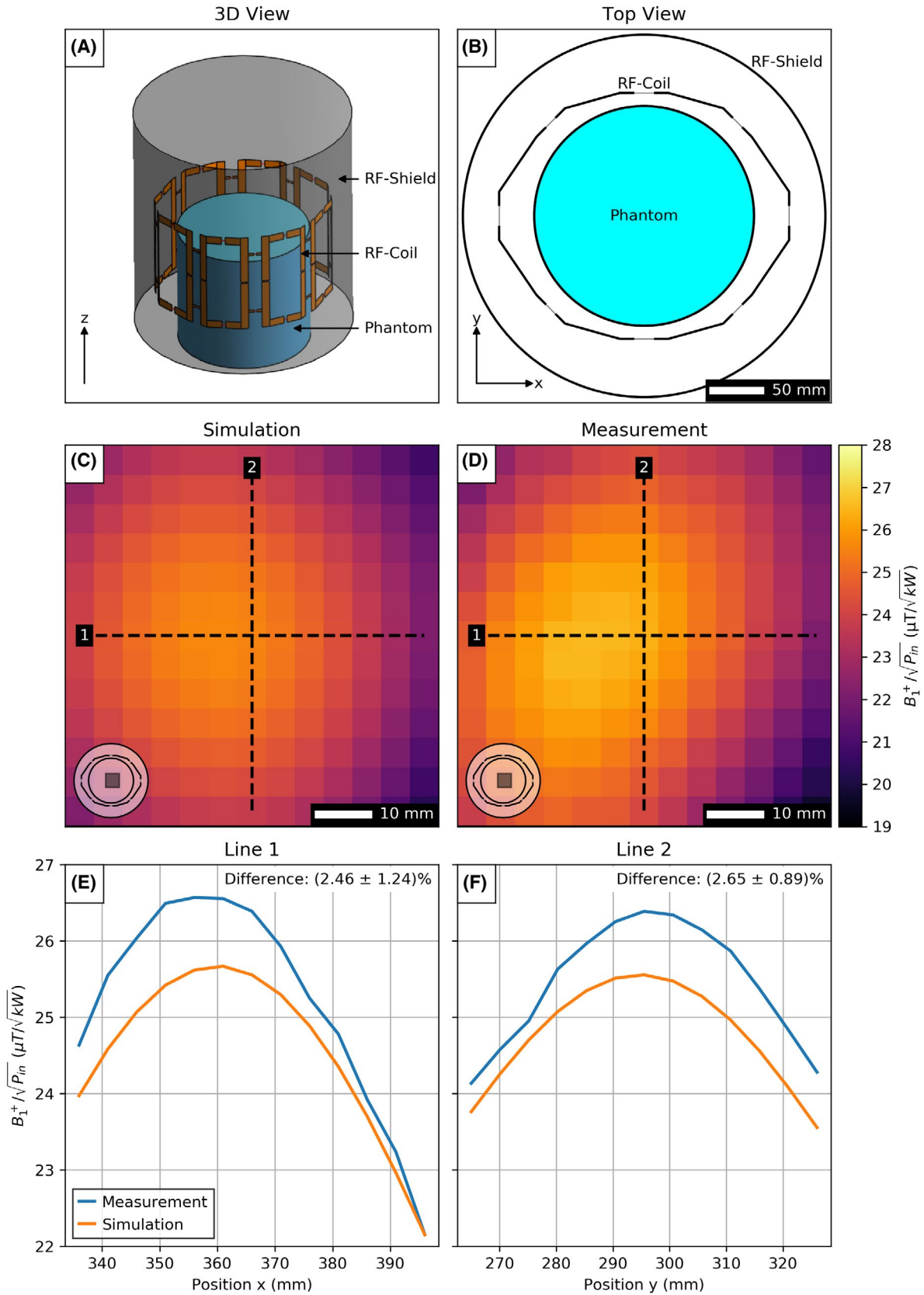


**FIGURE 5** Comparison of the measured and simulated  $B_1^+$  fields at 297 MHz. A, 3D view and (B) top view of the simulation setup depicting the RF coil, RF coil shielding and phantom. C, simulated and (d)  $B_1^+$  field inside the phantom in a  $(60 \text{ mm} \times 60 \text{ mm})$  x-y slice measured on a 5 mm square grid. Simulation results extracted from (C) and (D) across a (E) horizontal and (F) vertical line

**FIGURE 6** Comparison of fiber optic temperature probe measurements and thermistor measurements. Please note that the small irregularities visible for the thermistor temperature measurement (blue arrows) are due to short intended interrupts of the RF power source and not due to limitations of the measurement procedure

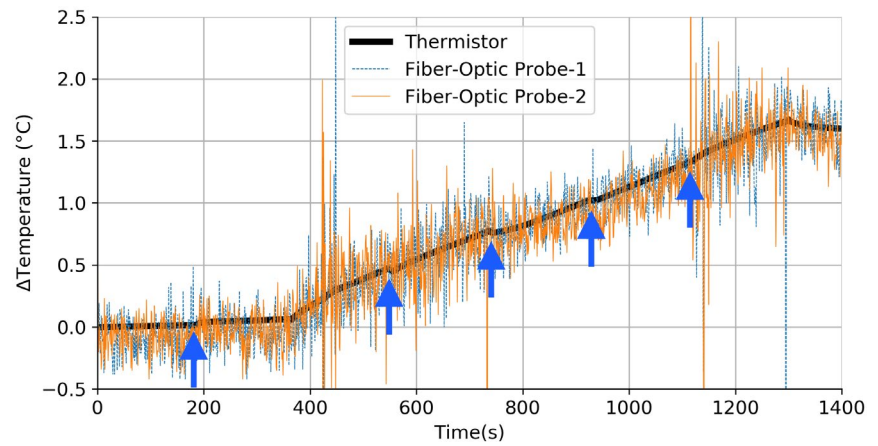
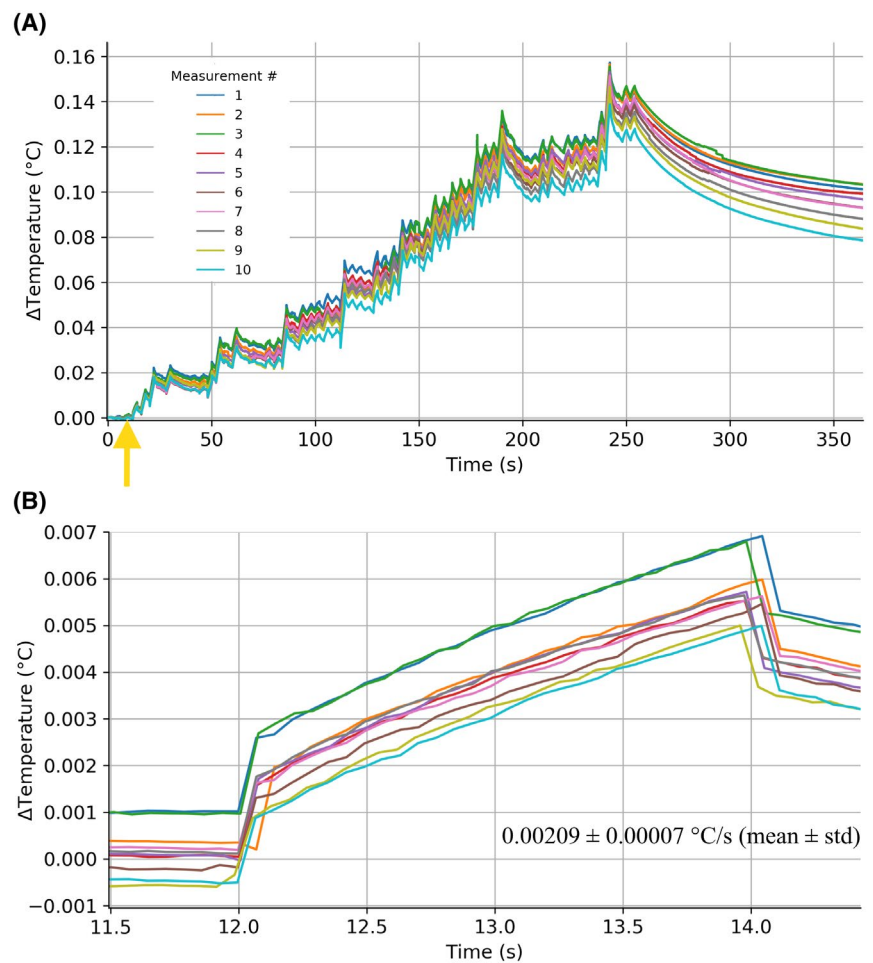


**FIGURE 7** A, Ten consecutive thermistor temperature measurements of an RF heating experiment of 64 consecutive 2s RF pulses each followed by 2s cooling. Different pTx transmission configurations (driving voltages) are applied in each pulse resulting in different RF fields and temperature profiles at the guidewire tip. Very similar heating profiles could be deduced from this set of RF heating pulses. B, Zoomed version of the data after 12s (orange arrow) showing the achievable high temperature resolution during the short sampling time. For all ten measurements the slope for this RF heating pulse is visible and can be evaluated with consistent results (mean  $\pm$  std of  $0.00209^{\circ}\text{C}/\text{s} \pm 0.00007^{\circ}\text{C}/\text{s}$ )



method to investigate multiple guidewire positions inside the phantom for multiple exposure scenarios.

The repeatability of the temperature measurements was investigated by exposing the guidewire at a fixed location to a sequence of 64 pTx pulses with varying amplitudes and phases per channel (2s RF heating, 2s cool-down). The same sequence was repeated ten times. The resulting, complex temperature curves are displayed in Figure 7 and indicate a good repeatability for all these measurements (Figure 7A).

The increase of the baseline temperature at the tip is very low ( $\Delta T \approx 0.1^{\circ}\text{C}$  per cycle). Still, this means a temperature difference between tip and phantom bulk builds up over time, resulting in slightly higher cooling rates for higher measurement numbers. Figure 7B shows ten times the system response to a single RF pulse, indicating the precision ( $\lesssim 100 \mu\text{K}$ ) of the thermistor temperature measurements even at a sampling rate of  $\sim 14 \text{ s}^{-1}$ . Within such short RF heating duration, heat dissipation due to thermal conduction is

small and heating rates  $dT/dt$  can reliably be determined. In the case of Figure 7B, for instance, we consistently obtain  $dT/dt = 2.1$  mK/s with a standard deviation of  $\pm 3.3\%$  over ten measurements. Figure 7B also reveals RF artifacts, seeming temperature jumps of  $\sim 0.15$  mK at the beginning and end of each heating pulse, which were not completely suppressed by the low pass filters. These detrimental effects were small, however, and the affected data points could easily be discarded in the calculation of the slopes.

### 3.3 | Mitigation of RF induced currents and tip heating using pTx

The results for the mitigation of RF induced heating using time-domain  $E$ -field sensors are displayed in Figure 8 for three representative implant positions (labelled P1, P2, P3). The complex  $E$ -fields measured at each location show a unique  $\vec{S}_{TDS}$  vector indicating the position dependent contributions of each channel to the total  $E$ -field. Using these values, the worst-case and orthogonal projection modes were calculated and applied. The measured  $E$ -field amplitudes for each Tx mode and position are summarized in Table S2 and illustrated in Figure 8. As to be expected, the maximum induced  $E$ -field was always found for the WC mode and the minimum induced  $E$ -field for the OP mode. Compared to CP excitation the OP mode reduces the local  $E$ -field by at least a factor of 2.2 and interestingly the highest reduction factor of 3.8 is found at P2 where  $E_{CP}$  has already the lowest value (Table S2).

Even though the  $E$ -field mitigation occurred 65 mm away, the temperature rise at the tip after 77s of RF heating is also substantially reduced in OP mode (compared to CP) for all three positions with reduction factors from 3.0 to 4.8 (Table S2). Noteworthy is that the highest reduction factor and lowest absolute value for  $\Delta T$  in OP mode are found at P3 and not where the  $E$ -field suppression worked best (P2).

To extend these results and investigate more guidewire locations, measurements were performed in 5-mm steps within a 2D area of 100 mm  $\times$  50 mm. The results are displayed in Figure 9. As expected from the CP mode data, local  $E$ -field minima exist. This was previously shown with linearly polarized birdcage coils and used as a strategy to reduce RF induced heating of guidewires.<sup>55</sup> The WC mode has the strongest induced  $E$ -fields off-center when the guidewire is closer to the RF coil elements. The OP mode reduces the  $E$ -field values everywhere in the 2D slice (Figure 9), demonstrating the effectiveness of pTx pulse mitigation. At selected locations the OP mode reduced the induced  $E$ -field by a factor of 26 compared to the CP and by a factor of 55 compared to the WC mode (Figure 9). Overall, the OP mode reduced the  $E$ -fields by factors  $>2$  in 88% of the mapped area when

compared to CP excitation, and in 14% of all positions even by factors  $>5$ .

### 3.4 | pTx mitigation and imaging at 3T

The  $\vec{S}_{TDS}$  vector was successfully acquired along the coaxial cable and WC, CP and OP mode induced  $E$ -fields were evaluated (Figure 3D-E). For all positions along the cable OP was significantly reduced versus WC and CP (Figure 3E) and the corresponding RF induced heating (based on  $\vec{S}_{TDS}$  values 90mm away from the tip, arrow Figure 3D) showed substantially lower tip heating (Figure 3F). The OP method was furthermore successfully tested within the commercial 8-channel pTx system in MR experiments using a standard GRE sequence (Figure 10). RF induced values of the GRE sinc pulse were recorded with the  $E$ -field probes (Figure 10C) and used to determine  $\vec{S}_{TDS}$  and OP transmission mode, which was then used in MR imaging (Figure 10A,B) and RF heating experiments (Figure 10D).

## 4 | DISCUSSION

This work implemented and evaluated a parallel-transmit medical implant RF-safety testbed and demonstrated the feasibility of real-time mitigation of RF heating using pTx and time-domain  $E$ -field sensor measurements.

The sampling rate support experiments covering the whole range of relevant MRI field strengths from  $B_0 = 0.5T$  to  $B_0 = 7T$ .

The safety testbed showed a repeatability with a standard deviation  $<3\%$  for  $E$ -field measurements, when the guidewire was repositioned between measurements.  $B_1^+$  validation measurements revealed an RMSE of 6.3% between electromagnetic field simulations and  $H$ -field probe measurement. The field uncertainty of the TEM cell calibration, which includes all system uncertainties except the RF coil and the receiver is 5% (Table S1).

It was demonstrated that real-time pulse mitigation is feasible using time-domain  $E$ -field sensors and a home-built pTx system to reduce RF induced currents and RF induced heating via the OP method at 3T and 7T. The OP method is fast ( $\sim 1.3$  ms) allowing a real-time implementation and requires low peak power ( $\sim 1.4$  W) pulses, making it potentially applicable in vivo since low flip angle transmission is sufficient to calculate the OP mode. OP mode generation is based on the ‘worst-case’ vector, which is the dominant but not necessarily the only unit vector that creates tip heating. To reduce the tip current further the full coupling matrix could be determined for multiple sensor positions along the coaxial cable and the transmit weights could be adjusted based on a linear combination of ‘null modes’.<sup>26</sup> However, a realization with multiple sensor positions is challenging. Ideally sensor-based measurements are performed at or very

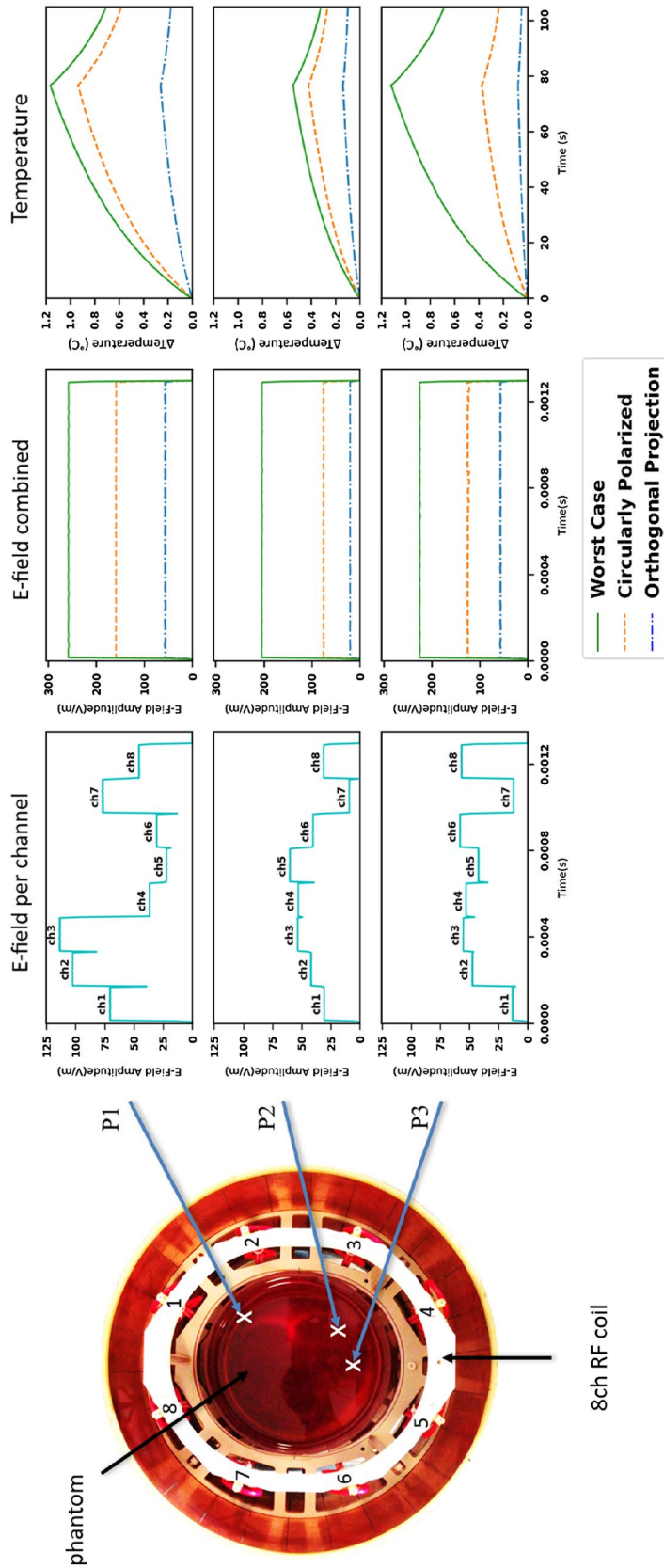


**FIGURE 8** E-fields and temperatures recorded at three arbitrary implant positions (rows). The first column shows the measured E-fields (only magnitudes are displayed) for the respective position (P1, P2, P3) when consecutively one coil element after the other is excited with the same voltage. From this data, which takes about 1 ms to acquire, the driving conditions “worst-case” (WC) mode and the “orthogonal projection” (OP) mode at the respective position of the E-field sensor can be calculated. Measured E-field amplitudes at the sensor position and corresponding heating curves at the tip are displayed in the center and rightmost column, respectively, for different excitation modes. As expected, the WC mode shows higher and the OP mode substantially reduced E-fields, when compared to circularly polarized (CP) excitation (central column). In the third column it is shown that the temperatures at the tip follow this behavior: most notably, the temperature rise at the tip is reduced by factors of 3 to 4 in the OP mode, even though the ‘mitigation point’ (E-field sensor) is 65 mm away

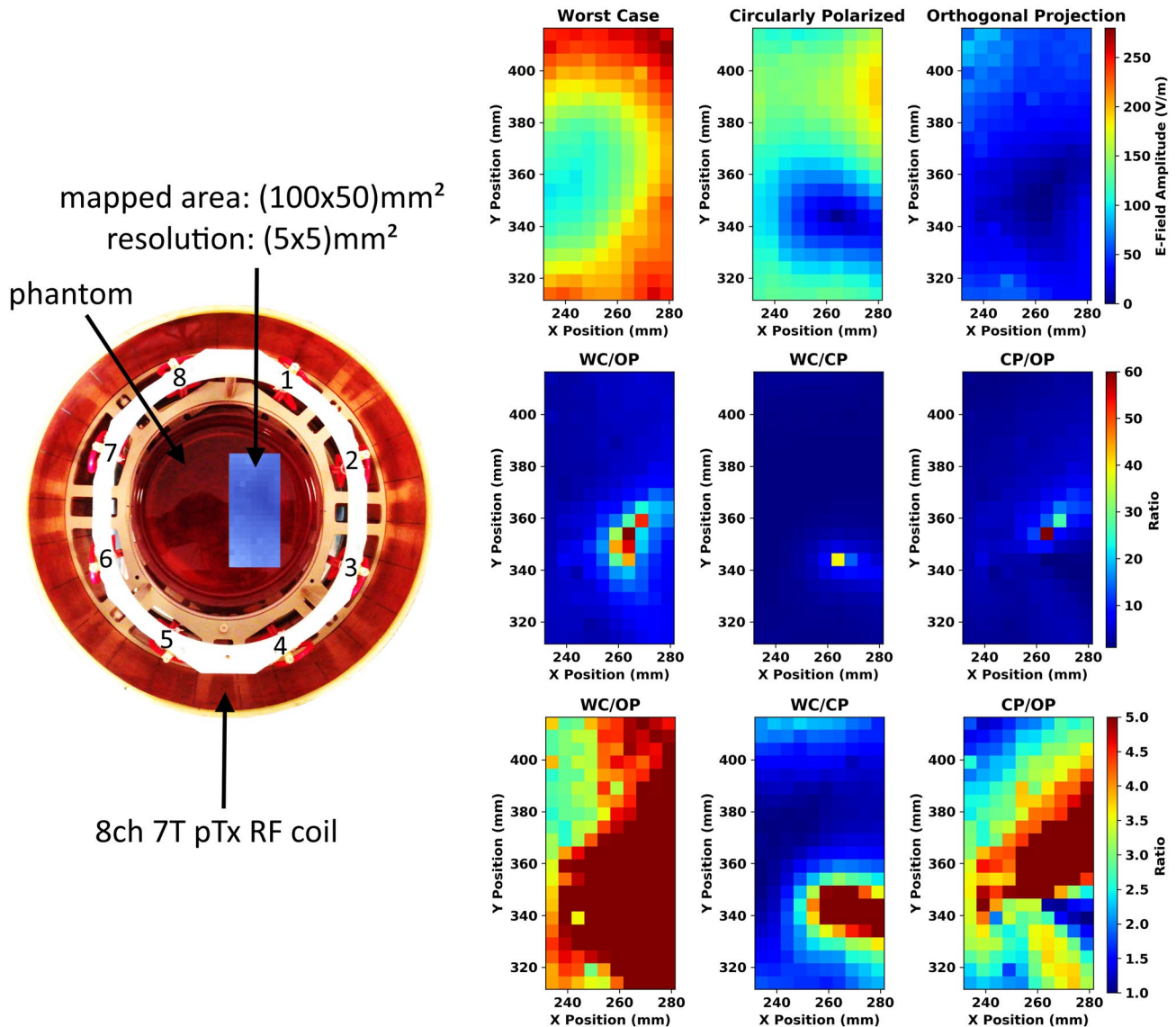


**FIGURE 9** E2D E-field mapping (resolution =  $5 \text{mm} \times 5 \text{mm}$ ) results for circularly polarized (CP), worst case (WC) and orthogonal projection (OP) excitation in an area of  $(100 \text{mm} \times 50 \text{mm})$  in the phantom. Excitation power (rms) was  $1.4 \text{W}$  in all cases. Results for each mode are shown in the top row while the mode ratios are shown in full-scale in the center row and on a zoomed scale in the bottom row. The OP mode can reduce induced E-fields at the wire by a factor of  $>26$  compared to the CP mode and  $>55$  compared to the WC mode. Furthermore, the OP mode reduces the induced E-fields by a factor of  $>2$  everywhere in the mapped area if compared to the WC mode and at 88% of all positions if compared to the CP mode. It may also be noteworthy that moving the guidewire by only  $5 \text{mm}$  can change the E-field amplitude by more than a factor five (CP mode)

close to the tip. In addition to RF heating mitigation, the OP mode is also based on a transmission vector used for imaging (eg, CP or any other imaging mode). This allows tip heating reduction of an implant, while at the same time sufficient  $B_1^+$  quality is maintained for imaging outside the implant location (Figures 4 and 10). The presented OP technique needs to be further benchmarked against other pTx mitigation techniques.<sup>26,51</sup>

It was shown for the 7T setup, that the induced E-fields were reduced in the whole investigated area and not only in selected locations. In 88% of the investigated area a reduction

factor of more than 2 was measured for the OP mode compared to CP excitation. In 14% of the investigated positions even a reduction by factors  $>5$  was observed, with an overall maximum reduction factor of 26. This demonstrates that in combination with real-time sensor feedback from the implant, pTx systems can efficiently be used to mitigate RF induced heating. It is important to note that this sensor-pTx combination provides an independent, self-contained hazard management; in principle, the approach is capable to ensure safe scanning of the patient without any ex ante investigation of the implant by simulations or in-vitro testing. This independence

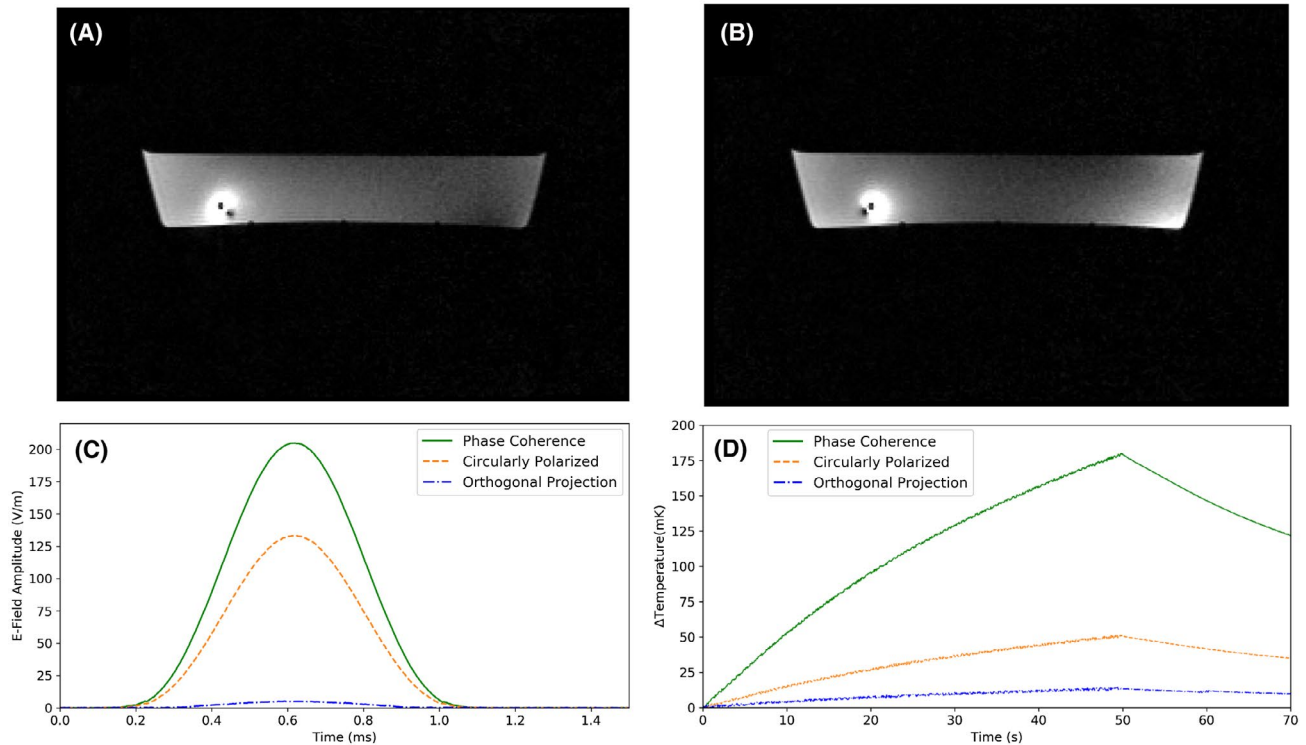


**FIGURE 10** Axial GRE images (spatial resolution =  $1.2 \text{ mm} \times 1.2 \text{ mm} \times 5.0 \text{ mm}$ ), TR = 7.8 ms, TE = 3.06 ms, averages = 2) at 3T in (A) CP and (B) OP pTx mode acquired with an 8-channel pTx RF coil and an 8-channel pTx system (Siemens Healthineers, Erlangen, Germany). The imaging artifact shows the location of the coaxial cable. C, Induced E-field values measured for a phase coherent ( $\vec{S}_{TDS}$  based phases and equal amplitudes), CP and OP mode transmission with a GRE sequence (sinc pulse) at the coaxial cable at a distance of 110mm from the tip. All three modes were transmitting with the same forward power. D, corresponding temperature curves for RF induced tip heating performed with the three pTx transmission modes. OP is able to substantially reduce RF induced heating compared to CP. Please note that for MR imaging experiments, the E-field sensor was removed and the E-field sensor electronics as well as the electronics from the positioning system were switched off in order to reduce noise

is an important feature since all three methods, simulations, in vitro testing and the real-time measurements proposed here, are prone to errors that might have tremendous implications on the actual amount of RF heating in vivo. Our data show, for instance, that moving the guidewire by only a few millimeters can change the induced E-field amplitude by a factor  $>5$  (CP, Figure 9). Even though the E-field measurements are only indirectly coupled to the tip heating, severe variations must also be expected in terms of tip heating when the guidewire location is changed by only a few millimeters. This effect needs further attention in future studies. An on-the-fly comparison of forward predictions, from simulations and in-vitro testing, with real-time sensor feedback during the MRI scan has the potential to reduce the chance for implant-related accidents in MRI substantially. In particular the sensitivity ( $\sim 100 \mu\text{K}$ ) and sampling speed ( $\sim 14 \text{ Hz}$ ) of thermistors would allow for such real-time feedback<sup>56</sup> and might even be capable to modify the pTx excitation mode based on temperature measurements alone.<sup>57,58</sup> Fast and still accurate 2D and 3D temperature measurements in phantoms are possible, while the widely used fiber-optic temperature probes need longer RF heating durations with higher magnitudes to compensate

for their limited precision. This has the additional advantage that the background temperature of the phantom is lower (such as the temperature gradient between the phantom and its surrounding), making both the experiments and the modelling easier and less error-prone. The relatively long cable connecting guidewire and multimeter could be replaced by a wireless transmission, reducing coupling artefacts and allowing measurements of smaller and shorter implants.<sup>14,56,59,60</sup>

Our CP, OP and WC mode results are related to transmitted forward power, which was calibrated beforehand using the TEM cell. In order to improve the evaluation based on total delivered power, forward and reverse power monitoring during RF heating needs to be implemented.

At present, our mapping experiments are limited due to the E-field sensor size and orientation. Time-domain E-field sensors are also very location and orientation sensitive making it difficult to get accurate absolute results and relate the readings directly to tip SAR. For that purpose, current sensors might be better suited.<sup>26</sup> Furthermore, there is a shielding effect present due to the guidewire, suggesting that the measurement results (in terms of absolute values) could be improved by mapping multiple E-field

locations. This would be also needed in case of sensor measurements at current null positions, which do not necessarily show a tip current null, eg, due to wavelength effects.<sup>26</sup> Notwithstanding these challenges of a quantitative assessment, it was demonstrated that  $E$ -field readings can successfully be used for a substantial pTx mitigation of implants, while current sensors are limited to interventional devices or need to be embedded in the implant,<sup>26,61</sup>  $E$ -field sensors can be applied externally even to more complex implant geometries, thus greatly increasing the variety of investigated implant safety testing.

The pTx system was demonstrated to be operational with one specific clinical 3T MRI. The operability of the system within the MR environment depends on multiple factors, however, such as space or stray field, which vary between sites. Both the home-built and vendor-provided pTx system were successfully used to apply the orthogonal projection for pTx mitigation and imaging (Figures 3 and 10). Such setups hold the promise to validate MR based methods proposed for in vivo assessments of implant safety, eg, via  $B_1^+$  or image based current detection methods<sup>17,19,23,62,63</sup> or MR thermometry.<sup>20</sup> Other applications include the measurement of the transfer function<sup>15</sup> or validation experiments of the MR based transfer matrix.<sup>22</sup> Moreover, pTx applications beyond the implant safety domain would benefit from a scalable, adjustable multi-frequency parallel transmit system such as X-nuclei imaging or thermal magnetic resonance.<sup>64,65</sup>

As the total number of possible configurations and combinations in medical device testing can be very large,<sup>66</sup> enabling relatively fast high resolution mapping of various locations and orientations of medical devices is crucial to advance the field and complementary to what is possible and recommended in performing numerical simulations.<sup>67</sup>

## 5 | CONCLUSION

To summarize, the presented open source parallel-transmit medical implant RF-safety testbed provides a hardware configuration for the assessment of implant safety in and outside the MR scanner for (a) comprehensive investigations of various implant safety scenarios, (b) validation studies of simulations or MR based implant safety methods, (c) the development of pTx based mitigation strategies, and (d) to increase the availability and access to pTx technology for a variety of other non-safety related applications. The real-time pTx mitigation strategies applying time-domain  $E$ -field sensors and the orthogonal projection mode show encouraging phantom results to reduce RF induced tip. Based on our results it seems feasible to implement a feedback loop where sensors on the medical implant communicate with a pTx-capable MR scanner. This approach would remove the responsibility for

safe implant scanning away from the MR operator and simultaneously support implant manufactures since an additional, independent safety watchdog becomes available, complementing ex ante assessments based on simulations and in-vitro testing by a sufficiently fast supervision system.

## ACKNOWLEDGMENTS

This work was funded by the EMPIR grant 17IND01 MIMAS. The EMPIR initiative is co-funded by the European Union's Horizon 2020 research and innovation program and the EMPIR participating states.

## ORCID

Lukas Winter  <https://orcid.org/0000-0002-4381-275X>

Berk Silemek  <https://orcid.org/0000-0001-8227-3632>

Johannes Petzold  <https://orcid.org/0000-0001-9503-0998>

Bernd Ittermann  <https://orcid.org/0000-0002-4087-471X>

## REFERENCES

1. Marwick C. Implant recommendations. *JAMA*. 2000;283:869.
2. Mosher ZA, Sawyer JR, Kelly DM. MRI safety with orthopedic implants. *Orthop Clin North Am*. 2018;49:455-463.
3. Winter L, Oberacker E, Özerdem C, et al. On the RF heating of coronary stents at 7.0 Tesla MRI. *Magn Reson Med*. 2015;74:999-1010.
4. Santoro D, Winter L, Müller A, et al. Detailing radio frequency heating induced by coronary stents: a 7.0 Tesla magnetic resonance study. *PLoS One*. 2012;7:e49963.
5. Kraff O, Wrede KH, Schoemberg T, et al. MR safety assessment of potential RF heating from cranial fixation plates at 7 T. *Med Phys*. 2013;40:042302.
6. Shellock FG, Fieno DS, Thomson LJ, Talavage TM, Berman DS. Cardiac pacemaker: in vitro assessment at 1.5 T. *Am Heart J*. 2006;151:436-443.
7. Golestanirad L, Rahsepar AA, Kirsch JE, et al. Changes in the specific absorption rate (SAR) of radiofrequency energy in patients with retained cardiac leads during MRI at 1.5T and 3T. *Magn Reson Med*. 2019;81:653-669.
8. Baker KB, Tkach JA, Phillips MD, Rezaei AR. Variability in RF-induced heating of a deep brain stimulation implant across MR systems. *J Magn Reson Imaging*. 2006;24:1236-1242.
9. Golestanirad L, Angelone LM, Iacono MI, Katnani H, Wald LL, Bonmassar G. Local SAR near deep brain stimulation (DBS) electrodes at 64 and 127 MHz: a simulation study of the effect of extracranial loops. *Magn Reson Med*. 2017;78:1558-1565.
10. Prescott JH, Lipka S, Baldwin S, et al. Chronic, programmed polypeptide delivery from an implanted, multireservoir microchip device. *Nat. Biotechnol*. 2006;24:437-438.
11. ASTM F2182-11a A. Standard test method for measurement of radio frequency induced heating on or near passive implants during magnetic resonance imaging. 2019.
12. ISO/TS 10974 S. Assessment of the safety of magnetic resonance imaging for patients with an active implantable medical device. 2018;10974.
13. Yeung CJ, Susil RC, Atalar E. RF safety of wires in interventional MRI: using a safety index. *Magn Reson Med*. 2002;47:187-193.

14. Acikel V, Atalar E. Modeling of radio-frequency induced currents on lead wires during MR imaging using a modified transmission line method. *Med Phys*. 2011;38:6623-6632.
15. Park S-M, Kamondetdacha R, Nyenhuis JA. Calculation of MRI-induced heating of an implanted medical lead wire with an electric field transfer function. *J Magn Reson Imaging*. 2007;26:1278-1285.
16. Ellenor CW, Stang PP, Etezadi-Amoli M, Pauly JM, Scott GC. Offline impedance measurements for detection and mitigation of dangerous implant interactions: an RF safety prescreen. *Magn Reson Med*. 2015;73:1328-1339.
17. van den Bosch MR, Moerland MA, Legendijk JJ, Bartels LW, van den Berg CA. New method to monitor RF safety in MRI-guided interventions based on RF induced image artefacts. *Med Phys*. 2010;37:814-821.
18. Gensler D, Fidler F, Ehses P, et al. MR safety: Fast T1 thermometry of the RF-induced heating of medical devices. *Magn Reson Med*. 2012;68:1593-1599.
19. Griffin GH, Anderson KJ, Celik H, Wright GA. Safely assessing radiofrequency heating potential of conductive devices using image-based current measurements. *Magn Reson Med*. 2015;73:427-441.
20. Winter L, Oberacker E, Paul K, et al. Magnetic resonance thermometry: methodology, pitfalls and practical solutions. *Int J Hyperthermia*. 2016;32:63-75.
21. Tokaya JP, Raaijmakers AJE, Luijten PR, Bakker JF, van Den Berg CA. MRI-based transfer function determination for the assessment of implant safety. *Magn Reson Med*. 2017;78:2449-2459.
22. Tokaya JP, Raaijmakers AJ, Luijten PR, van den Berg CA. MRI-based, wireless determination of the transfer function of a linear implant: Introduction of the transfer matrix. *Magn Reson Med*. 2018;80:2771-2784.
23. Eryaman Y, Kobayashi N, Moen S, et al. A simple geometric analysis method for measuring and mitigating RF induced currents on Deep Brain Stimulation leads by multichannel transmission/reception. *NeuroImage*. 2019;184:658-668.
24. Eryaman Y, Turk EA, Oto C, Algin O, Atalar E. Reduction of the radiofrequency heating of metallic devices using a dual-drive birdcage coil. *Magn Reson Med*. 2013;69:845-852.
25. Gudino N, Sonmez M, Yao Z, et al. Parallel transmit excitation at 1.5 T based on the minimization of a driving function for device heating. *Med Phys*. 2015;42:359-371.
26. Etezadi-Amoli M, Stang P, Kerr A, Pauly J, Scott G. Controlling radiofrequency-induced currents in guidewires using parallel transmit. *Magn Reson Med*. 2015;74:1790-1802.
27. McElcheran CE, Yang B, Anderson KJ, Golestanirad L, Graham SJ. Investigation of parallel radiofrequency transmission for the reduction of heating in long conductive leads in 3 Tesla magnetic resonance imaging. *PLoS One*. 2015;10:e0134379.
28. Weidemann G, Seifert F, Ittermann B. Reduction of the E field at the tip of implanted wires generated by PTx coils using RF current measurements. *Proc Int Soc Mag Reson Med; Singapore*. 2016;2216-.
29. Eryaman Y, Guerin B, Akgun C, et al. Parallel transmit pulse design for patients with deep brain stimulation implants. *Magn Reson Med*. 2015;73:1896-1903.
30. Bachschmidt TJ, Köhler M, Nistler J, Geppert C, Jakob PM, Nittka M. Polarized multichannel transmit MRI to reduce shading near metal implants. *Magn Reson Med*. 2016;75:217-226.
31. McElcheran CE, Yang B, Anderson KJ, Golestanirad L, Graham SJ. Parallel radiofrequency transmission at 3 tesla to improve safety in bilateral implanted wires in a heterogeneous model. *Magn Reson Med*. 2017;78:2406-2415.
32. McElcheran CE, Golestanirad L, Iacono MI, et al. Numerical simulations of realistic lead trajectories and an experimental verification support the efficacy of parallel radiofrequency transmission to reduce heating of deep brain stimulation implants during MRI. *Sci Rep*. 2019;9:2124-2138.
33. Vaughan T, Delabarre L, Snyder C, et al. 9.4T human MRI: preliminary results. *Magn Reson Med*. 2006;56:1274-1282.
34. Feng K, Hollingsworth NA, McDougall MP, Wright SM. A 64-channel transmitter for investigating parallel transmit MRI. *IEEE Trans Biomed Eng*. 2012;59:2152-2160.
35. Orzada S, Solbach K, Gratz M, et al. A 32-channel parallel transmit system add-on for 7T MRI. *PLoS One*. 2019;14:e0222452.
36. Seifert F, Pfeiffer H, Mecke R, Waxmann P, Ittermann B. 7T 8-Channel PTx head coil with high B1+ efficiency optimized for MRS. *Proc Int Soc Mag Reson Med; Singapore*. 2016;3545-.
37. Ianniello C, de Zwart JA, Duan QI, et al. Synthesized tissue-equivalent dielectric phantoms using salt and polyvinylpyrrolidone solutions. *Magn Reson Med*. 2018;80:413-419.
38. Brink WM, Wu Z, Webb AG. A simple head-sized phantom for realistic static and radiofrequency characterization at high fields. *Magn Reson Med*. 2018;80:1738-1745.
39. Wagner F, Laun FB, Kuder TA, et al. Temperature and concentration calibration of aqueous polyvinylpyrrolidone (PVP) solutions for isotropic diffusion MRI phantoms. *PLoS One*. 2017;12:e0179276.
40. Keenan KE, Wilmes LJ, Aliu SO, et al. Design of a breast phantom for quantitative MRI. *J Magn Reson Imaging*. 2016;44:610-619.
41. Taber KH, Hayman LA. Temperature monitoring during MR imaging: comparison of fluoroptic and standard thermistors. *J Magn Reson Imaging*. 1992;2:99-101.
42. Kangarlu A, Tang L, Ibrahim TS. Electric field measurements and computational modeling at ultrahigh-field MRI. *Magn Reson Imaging*. 2007;25:1222-1226.
43. Nordbeck P, Fidler F, Weiss I, et al. Spatial distribution of RF-induced E-fields and implant heating in MRI. *Magn Reson Med Off J Int Soc Magn Reson Med*. 2008;60:312-319.
44. Saniour I, Gaborit G, Perrier A-L, et al. Electro-optic probe for real-time assessments of RF electric field produced in an MRI scanner: feasibility tests at 3 and 4.7 T. *NMR Biomed*. 2018;31:e3849.
45. Weidemann G, Seifert F, Hoffmann W, Pfeiffer H, Seemann R, Ittermann B. Measurements of RF power reflected and radiated by multichannel transmit MR coils at 7T. *Magn Reson Mater Phys Biol Med*. 2016;29:371-378.
46. ISO/TR 21900. Guidance for uncertainty analysis regarding the application of ISO/TS 10974. 2018.
47. Han H, Moritz R, Oberacker E, Waiczies H, Niendorf T, Winter L. Open source 3D multipurpose measurement system with submillimetre fidelity and first application in magnetic resonance. *Sci Rep*. 2017;7:13452.
48. Klepsch T, Linde TD, Hoffmann W, Botterweck H, Ittermann B, Seifert F. Calibration of fibre-optic RF E/H-field probes using a magnetic resonance (MR) compatible TEM cell and dedicated MR measurement techniques. *Biomed Eng Biomed Tech*. 2012;57:119-122.
49. Graesslin I, Krueger S, Vernickel P, Achtzehn J, Nehrke K, Weiss S. Detection of RF unsafe devices using a parallel transmission MR system. *Magn Reson Med*. 2013;70:1440-1449.

50. Graesslin I, Vernickel P, Börner P, et al. Comprehensive RF safety concept for parallel transmission MR. *Magn Reson Med*. 2015;74:589-598.
51. Godinez F, Scott G, Padormo F, Hajnal JV, Malik SJ. Safe guide-wire visualization using the modes of a PTx transmit array MR system. *Magn Reson Med*. 2020;83:2343-2355.
52. Seifert F, Weidemann G, Ittermann B. Q Matrix approach to control implant heating by transmit array coils. *Proc Int Soc Mag Reson Med; Toronto, Ontario, Canada*. 2015;3212.
53. Christ A, Kainz W, Hahn EG, et al. The Virtual Family—development of surface-based anatomical models of two adults and two children for dosimetric simulations. *Phys Med Biol*. 2010;55:N23-N38.
54. ITIS Foundation. EM and thermal tissue parameter database. Retrieved from <https://itis.swiss/virtual-population/tissue-properties/database/database-summary/>. Accessed October 2, 2019.
55. Eryaman Y, Akin B, Atalar E. Reduction of implant RF heating through modification of transmit coil electric field. *Magn Reson Med*. 2011;65:1305-1313.
56. Özen AC, Silemek B, Lottner T, Atalar E, Bock M. MR safety watchdog for active catheters: wireless impedance control with real-time feedback. *Magn Reson Med*. 2020;84:1048-1060.
57. Silemek B, Winter L, Seifert F, Pfeiffer H, Ittermann B. Measurement based mitigation of RF related safety hazards of implants in parallel transmission using temperature matrix. In: *ISMRM Workshop on MR Safety*. Utrecht, Netherlands; 2019.
58. Silemek B, Winter L, Seifert F, Pfeiffer H, Ittermann B. Measurement-based safety assessment, prediction and mitigation of RF induced implant heating using parallel transmission: the temperature matrix. *Proc Int Soc Mag Reson Med; Virtual Meeting*. 2020: 69
59. Silemek B, Acikel V, Oto C, et al. A temperature sensor implant for active implantable medical devices for in vivo subacute heating tests under MRI. *Magn Reson Med*. 2018;79:2824-2832.
60. Acikel V, Silemek B, Atalar E. Wireless control of induced radiofrequency currents in active implantable medical devices during MRI. *Magn Reson Med*. 2020;83:2370-2381.
61. Etezadi-Amoli M, Stang P, Kerr A, Pauly J, Scott G. Interventional device visualization with toroidal transceiver and optically coupled current sensor for radiofrequency safety monitoring. *Magn Reson Med*. 2015;73:1315-1327.
62. Overall WR, Pauly JM, Stang PP, Scott GC. Ensuring safety of implanted devices under MRI using reversed RF polarization. *Magn Reson Med*. 2010;64:823-833.
63. Griffin GH, Ramanan V, Barry J, Wright GA. Toward in vivo quantification of induced RF currents on long thin conductors. *Magn Reson Med*. 2018;80:1922-1934.
64. Winter L, Özerdem C, Hoffmann W, et al. Design and evaluation of a hybrid radiofrequency applicator for magnetic resonance imaging and RF induced hyperthermia: electromagnetic field simulations up to 14.0 tesla and proof-of-concept at 7.0 tesla. *PLoS One*. 2013;8:e61661.
65. Winter L, Özerdem C, Hoffmann W, et al. Thermal magnetic resonance: physics considerations and electromagnetic field simulations up to 23.5 Tesla (1GHz). *Radiat Oncol*. 2015;10:201-212.
66. Food and Drug Administration (FDA). Assessment of radiofrequency-induced heating in the magnetic resonance (MR) environment for multi-configuration passive medical devices—guidance for industry and food and drug administration staff. 2016.
67. Yao A, Zastrow E, Kuster N. Robust experimental evaluation method for the safety assessment of implants with respect to RF-induced heating during MRI. In: *Proceedings of the 32nd International Union of Radio Science General Assembly and Scientific Symposium (URSI GASS)*. 2017.

## SUPPORTING INFORMATION

Additional Supporting Information may be found online in the Supporting Information section.

**FIGURE S1** Simulated E- and B-fields of the 8-channel 7T pTx RF coil in CP mode. (A)  $E_x$ , (B)  $E_y$  and (C)  $E_z$  field distribution in the x-y plane 50 mm below the phantom liquid surface. (D) line profile of the fields along the dotted-line indicates that at a distance of around  $\pm 20$  mm from the center  $E_z > E_y$ . (E)  $H_x$ , (F)  $H_y$  and (G)  $H_z$  field distribution and (H) line profile along the dotted line respectively. For the Hfields within the central area of  $\pm 20$  mm  $H_z \ll H_x < H_y$ , allowing accurate validation of the simulations in this area based on  $B_1^+$  measurements ( $B_x$  and  $B_y$ ) only

**TABLE S1** Uncertainties of components used in this study. \*Please note that the TEM cell uncertainty includes the overall system with E- and H-field probe and transmit chain uncertainties (except RF coil and receiver).

**TABLE S2** E-fields and temperatures measured at different positions and for different pTx excitation modes (see also Figure 8)

**How to cite this article:** Winter L, Silemek B, Petzold J, et al. Parallel transmission medical implant safety testbed: Real-time mitigation of RF induced tip heating using time-domain E-field sensors. *Magn Reson Med*. 2020;84:3468-3484. <https://doi.org/10.1002/mrm.28379>